AIAA JOURNAL
Vol. 50, No. 2, February 2012

Two-Dimensional Orthotropic Plate Analysis for an Integral Thermal Protection System

Oscar Martinez,* Bhavani Sankar,† and Raphael Haftka‡
University of Florida, Gainesville, Florida 32611
and
Max L. Blosser§
NASA Langley Research Center, Hampton, Virginia 23681

DOI: 10.2514/1.J051172

This paper is concerned with homogenization of a corrugated-core sandwich panel, which is a candidate structure for integrated thermal protection systems for space vehicles. The focus is on determining the local stresses in an integrated thermal protection system panel subjected to mechanical and thermal loads. A micromechanical method is developed to homogenize the sandwich panel as an equivalent orthotropic plate. Mechanical and thermal loads are applied to the equivalent thick plate, and the resulting plate deformations were obtained through a shear deformable plate theory. The two-dimensional plate deformations are used to obtain local integrated thermal protection system stresses through reverse homogenization. In addition, simple beam models are used to obtain local facesheet deformations and stress. The local stresses and deflections computed using the analytical method were compared with those from a detailed finite element analysis of the integrated thermal protection system. For the integrated thermal protection system examples considered in this paper, the maximum error in stresses and deflections is less than 5%. This was true for both mechanical and thermal loads acting on the integrated thermal protection system.

Nomenclature

a	=	integrated thermal protection system length
b	=	integrated thermal protection system width
d	=	height of sandwich panel (centerline to centerline)
$\bar{D}$	=	inverse bending stiffness matrix
D^*	=	reduced bending stiffness matrix
E	=	Young's modulus
EI	=	equivalent flexural rigidity
G	=	transverse shear modulus
P_z	=	pressure load acting on the two-dimensional orthotropic panel
$\{q\}$	=	displacement vector
Q_{ij}	=	transformed lamina stiffness matrix
Q_x, Q_y	=	shear force on unit cell
$\bar{Q}_{ij}$	=	transformed lamina stiffness matrix in the nonprincipal coordinate system
s	=	web length
t_{BF}	=	bottom facesheet thickness
t_{TF}	=	top facesheet thickness
t_w	=	web thickness
$[T_D]^{(e)}$	=	deformation transformation matrix of the ith component of the corrugated core
U	=	unit-cell strain energy
v	=	deflection of beam
w	=	integrated thermal protection system panel deflection
$\bar{y}_f$	=	local y axis of facesheet
$\bar{y}_w$	=	local y axis of web
$\bar{z}_f$	=	local z axis of facesheet
$\bar{z}_w$	=	local z axis of web
ε_o	=	midplane strain
θ	=	angle of web inclination
κ	=	curvature
λ	=	roots of auxiliary equation
ν	=	Poisson's ratio
ψ_x, ψ_y	=	rotations of the plate's cross section
$2p$	=	unit-cell length

I. Introduction

THE primary function of a thermal protection system (TPS) is to protect the space vehicle from extreme aerodynamic heating and to maintain the underlying structure within acceptable temperature and mechanical constraints [1]. The current state-of-the-art reusable TPS covers the outer surface of a vehicle with a layer that does not carry significant loads but prevents the underlying load-bearing structure from exceeding acceptable temperature limits.

An intriguing alternative is to embed the relatively fragile insulation in a structural load-bearing sandwich panel. A robust, structural facesheet would then form the outer surface of the vehicle, thereby potentially removing some vehicle operational constraints, e.g., flight through rain, and reducing required maintenance. By using the insulation thickness as a structural sandwich core, there is a potential to increase structural bending stiffness, save weight, and reduce overall thickness of the vehicle wall. There are significant challenges in designing a structure to function simultaneously as an efficient aerospace load-bearing structure and a thermal insulator. The challenges include understanding the key thermal-structural loads and requirements that drive the design, identifying materials that best perform in a thermal environment, and accommodating thermal expansion mismatches, thermal stresses, and effects of temperature-dependent properties inherent in these systems. Candidate concepts comprising metallic foams and innovative core materials, such as corrugated and truss cores, have been investigated.

The corrugated-core sandwich panel is composed of several unit cells placed adjacent to each other. The empty space in the corrugated core will be filled with a non-load-bearing insulation such as Safill®. The TPS concept combines all three passive TPS concepts: heat sink,

Received 13 January 2011; revision received 29 August 2011; accepted for publication 31 August 2011. Copyright © 2011 by the American Institute of Aeronautics and Astronautics, Inc. Copies of this paper may be made for personal or internal use, on condition that the copier pay the $10.00 per-copy fee to the Copyright Clearance Center, Inc., 222 Rosewood Drive, Danvers, MA 01923; include the code 0001-1452/12 and $10.00 in correspondence with the CCC.

*Structural Analyst, Department of Mechanical and Aerospace Engineering; Jacobs Engineering, Engineering Science Contract Group, Houston, Texas.

†Ebaugh Professor, Department of Mechanical and Aerospace Engineering. Associate Fellow AIAA.

‡Distinguished Professor, Department of Mechanical and Aerospace Engineering. Fellow AIAA.

§Aerospace Technologist, Metals and Thermal Structures Branch, Structural Concepts and Mechanics Branch.

hot structure, and insulated structure [2]. The sandwich structure will replace the structural skin and the insulation in the current thermal structures. Since the sandwich construction is stiffer than single skin construction, the number of frames and stringers will be significantly reduced. Furthermore, the insulation is protected from foreign object impact and requires less or no maintenance such as waterproofing. The integral TPS/structure [integrated thermal protection system (ITPS)] design (Fig. 1) can significantly reduce the overall weight of the vehicle as the TPS/structure performs the load-bearing function. The ITPS is expected to be multifunctional (offer insulation as well as load-bearing capability). Advantages of an ITPS concept have been identified by Martinez et al. [3].

The finite element method (FEM) is commonly used to perform three-dimensional (3-D) stress analysis of the ITPS structure. However, a full-scale 3-D finite element (FE) stress analysis will be expensive and time-consuming for a quick preliminary sizing analysis of an ITPS. The same is true with design optimization, which may involve 1000s of analyses. An alternative is to model the ITPS as an equivalent orthotropic plate and perform a 2-D plate analysis to obtain the displacement and stress fields.

This paper is the third in the sequel of papers written by the authors on the subject of homogenization of the ITPS. The procedures are depicted in Fig. 1a. The ITPS, which consists of repeating cells, is homogenized as an equivalent orthotropic plate, and the ABD matrices (stiffness matrices) of the equivalent plate are calculated using analytical methods. In the first paper [3], the authors described the homogenization procedures and verified the accuracy of the extensional [A], bending [D], and shear [C] stiffness matrices by comparing with those calculated using FEMs. In the second paper [4], procedures for calculating equivalent thermal forces and moments for a given through-the-thickness temperature distribution were developed without considering shear deformations. In the current paper, the equivalent orthotropic plate is analyzed using a first-order shear deformable theory in which the transverse shear stresses are not neglected. Both pressure loads and thermal loads are considered. The plate analysis results include midplane strains $\{\varepsilon_0\}$ and curvatures $\{\kappa\}$ at a given (x, y). Then, a reverse homogenization procedure is used to calculate the detailed stress field from the $\{\varepsilon_0\}$ and $\{\kappa\}$ obtained from the plate analysis. The stresses are compared with those obtained from a detailed 3-D analysis of the ITPS.

It is worth pointing out that, in the present work, analytical methods are used for every step of the procedures described above. Analytical methods are much faster than FE analysis and are suitable when 1000s of analyses have to be performed in the design optimization of the ITPS panel. Analytical methods will be extremely useful if one decides to use stochastic optimization rather than a safety-factor-based design approach.

Only a limited amount of work in micromechanical unit-cell analyses of sandwich structures is available in the literature [5–12]; it has been summarized in our previous works [3,4] and will not be repeated here. The aforementioned researchers used the force-distortion relationship, which involved mechanics of materials equations to determine average unit-cell stresses. In the current paper, we improve on that by use of a first-order shear deformable plate theory (FSDT) [13] for the 2-D equivalent ITPS plate analysis, reverse homogenization, and simple beam models for the local ITPS stress analysis. The higher-order theory that includes the effects of transverse shear deformation is suitable for an ITPS because of the significant transverse shear loads that are carried by the corrugated core. Although such stresses can be postcomputed through 3-D elasticity equilibrium equations, they are not always accurate. The classical laminate plate theory (CLPT) [14] underpredicts deflections and overpredicts buckling loads with plate length-to-thickness ratios less than 20. For this reason alone, it was necessary to use the

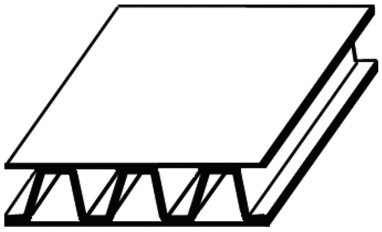

a)

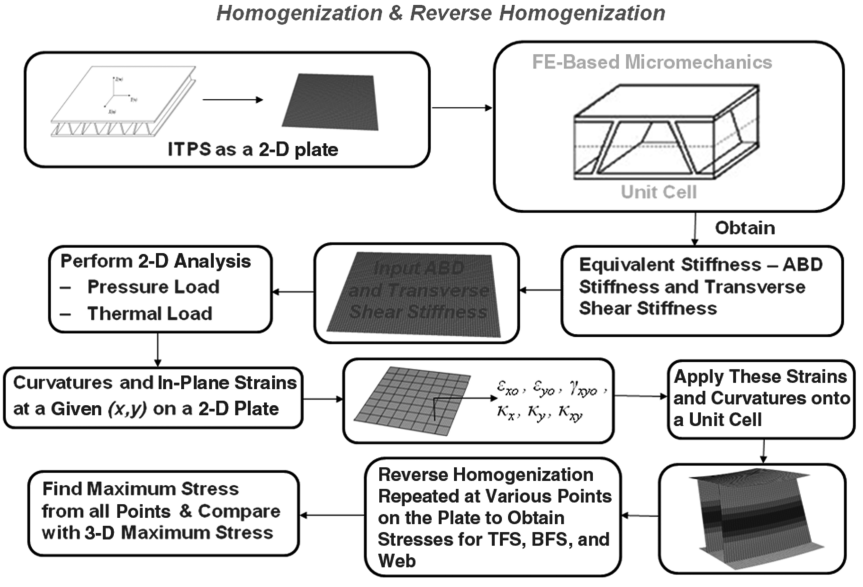

b)

Fig. 1 ITPS: a) corrugated-core sandwich panels for use as an ITPS and b) flowchart depicting procedures in homogenization of the ITPS panel and reverse homogenization to obtain the detailed displacements and stresses (TFS denotes top facesheet; BFS denotes bottom facesheet).

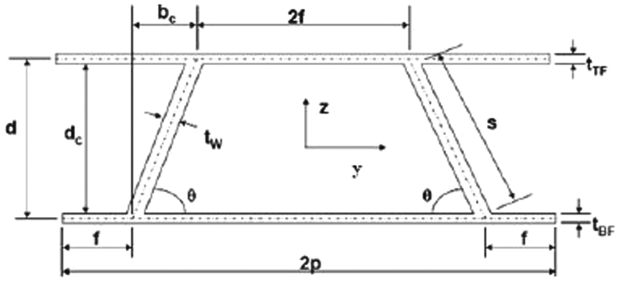

Fig. 2 Dimensions of the unit cell.

first-order theory in the ITPS analysis of relatively thick plates. The primary objective and importance of using the FSDT when analyzing the ITPS as a two-dimensional (2-D) homogenized plate was to bring out the effect of shear deformation on deflections and stresses.

The paper's objective is to derive a satisfactory approximate plate theory of an ITPS panel homogenized as a 2-D plate using the FSDT. The solution of the plate equations gives all necessary information for calculating stresses at any point of the thick plate. Local ITPS stresses of the facesheets and webs are derived by using the 2-D plate deflections w, rotations, ψ_x, ψ_y, reverse homogenization, and a transformation matrix. Reverse homogenization only captures the midplane strains and curvatures of the unit cell at the origin (see Fig. 2), which resulted in a uniform stress field in the facesheets and webs. Additional local analysis had to be done through one-dimensional (1-D) beam models to capture the nonuniform stress field of the facesheet and webs when subjected to mechanical and thermal loads. The ITPS panel is subjected to a uniform pressure load and thermal edge moments, and the resulting plate deflections and local ITPS stresses are compared with a detailed FE analysis of the ITPS.

II. Analysis

Consider a simplified geometry of an ITPS unit cell, shown in Fig. 2. The z axis is in the thickness direction of the ITPS panel. The stiffer longitudinal direction is parallel to the x axis, and the y axis is in the transverse direction. The unit cell consists of two inclined webs and two thin facesheets. The unit cell is symmetric with respect to the yz plane. The upper faceplate thickness t_{TF} can be different from the lower faceplate thickness t_{TB}, as well as the web thickness t_w. The unit cell can be identified by six geometric parameters $(p, d, t_{\mathrm{TF}}, t_{\mathrm{BF}}, t_w, \theta)$ (Fig. 2).

The equivalent stiffness of the orthotropic plate is obtained by comparing the behavior of a unit cell of the corrugated-core sandwich panel with that of an element of the idealized homogeneous orthotropic plate (Fig. 3).

The in-plane extensional and shear response and out-of-plane (transverse) shear response of the orthotropic panel are governed by the following constitutive relations:

$$\begin{bmatrix} N \\ Q \\ M \end{bmatrix} = \begin{bmatrix} [A] & [0_3] & [0_3] \\ [0_3] & [C] & [0_3] \\ [0_3] & [0_3] & [D] \end{bmatrix} \begin{Bmatrix} \varepsilon_o \\ \gamma \\ \kappa \end{Bmatrix} \quad \text{or} \quad \{F\} = [K]\{q\} \tag{1}$$

In Eq. (1), ε_o and γ are the in-plane and transverse shear strains, and κ are the bending and twisting curvatures; $\{N\}$, $\{Q\}$, and $\{M\}$, are the in-plane forces, transverse shear forces, and bending and twisting moments; and $[A]$, $[C]$, and $[D]$ are the extensional, transverse shear, and bending stiffness. The equivalent orthotropic plate is assumed to be symmetric about its midplane, leading to a negligible extension-bending coupling matrix $[B]$. The case of unsymmetric plates will be dealt with using approximate methods as discussed in this paper. The detailed homogenization procedures for determining the $[A]$, $[B]$, $[C]$, and $[D]$ matrices for the corrugated-core sandwich panel were derived in Martinez et al. [15]. In the following sections, we describe the procedures for determining the response of the ITPS to pressure and thermal loads.

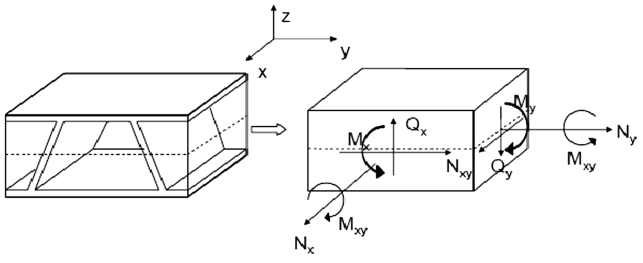

Fig. 3 Equivalent orthotropic thick plate for the unit cell of the corrugated-core sandwich panel.

A. Uniform Pressure Loading

A simply supported orthotropic sandwich panel of width b (y direction) and length a (x direction) was considered for a 2-D plate analysis (Fig. 3). The simply supported boundary conditions are described as

$$\begin{aligned} &w(0,y)=0, \quad w(a,y)=0 \quad M_x(0,y)=0 \\ &M_x(a,y)=0 \quad w(x,0)=0, \quad w(x,b)=0 \\ &M_y(x,0)=0, \quad M_y(x,b)=0 \end{aligned} \tag{2}$$

The panel is exposed to a uniform pressure load that can be represented by the double Fourier sine series, as shown in Eq. (3):

$$P_Z(x,y) = -\sum_{m=1}^{\infty}\sum_{n=1}^{\infty} P_{mn} \sin\left(\frac{m\pi x}{a}\right) \sin\left(\frac{n\pi y}{b}\right) \tag{3}$$

In the above equation, $P_{mn} = 16P_o/\pi^2 mn$ for uniform pressure loads [13], where P_o is the intensity of the uniformly distributed load. The ITPS panel is also assumed to have the following deformations that satisfy the simply supported boundary conditions:

$$w(x,y) = \sum_{m=1}^{\infty}\sum_{n=1}^{\infty} A_{mn} \sin\left(\frac{m\pi x}{a}\right) \sin\left(\frac{n\pi y}{b}\right) \tag{4a}$$

$$\psi_x(x,y) = \sum_{m=1}^{\infty}\sum_{n=1}^{\infty} B_{mn} \cos\left(\frac{m\pi x}{a}\right) \sin\left(\frac{n\pi y}{b}\right) \tag{4b}$$

$$\psi_y(x,y) = \sum_{m=1}^{\infty}\sum_{n=1}^{\infty} C_{mn} \sin\left(\frac{m\pi x}{a}\right) \cos\left(\frac{n\pi y}{b}\right) \tag{4c}$$

In the above equations, $w(x,y)$ is the out-of-plane displacement, and $\psi_x(x,y)$ and $\psi_y(x,y)$ are the plate rotations.

The unknown constants A_{mn}, B_{mn}, and C_{mn} were obtained by substituting the constitutive relations in the form of the assumed deformations from Appendix A [Eqs. (A2) and (A3)] into the differential equation of equilibrium [Eq. (A1)]. This results in a system of three linear equations for the unknown coefficients as shown:

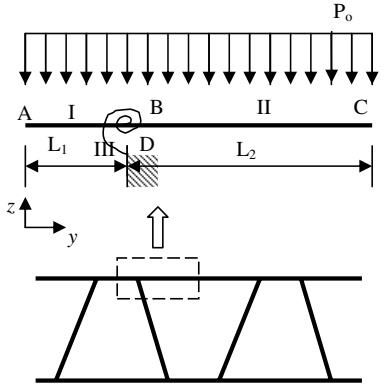

Fig. 4 Half of the top face under the action of a uniform pressure loading.

$$-\begin{bmatrix} D_{11}\left(\frac{m\pi}{a}\right)^2 + D_{66}\left(\frac{n\pi}{b}\right)^2 + kC_{55} & (D_{12}+D_{66})\left(\frac{mn\pi^2}{ab}\right) & kC_{55}\left(\frac{m\pi}{a}\right) \\ (D_{12}+D_{66})\left(\frac{mn\pi^2}{ab}\right) & D_{22}\left(\frac{n\pi}{b}\right)^2 + D_{66}\left(\frac{m\pi}{a}\right)^2 + kC_{44} & kC_{44}\left(\frac{n\pi}{b}\right) \\ kC_{55}\left(\frac{m\pi}{a}\right) & kC_{44}\left(\frac{n\pi}{b}\right) & kC_{55}\left(\frac{m\pi}{a}\right)^2 + kC_{44}\left(\frac{n\pi}{b}\right)^2 \end{bmatrix} \begin{Bmatrix} B_{mn} \\ C_{mn} \\ A_{mn} \end{Bmatrix} = \begin{Bmatrix} 0 \\ 0 \\ P_{mn} \end{Bmatrix} \tag{5}$$

After solving for the unknown constants, the deflections were obtained at a given (x, y) coordinate on the 2-D orthotropic sandwich panel using Eq. (4). The results in the above series converged for $m = n = 23$, resulting in a total of 529 terms in Eq. (4) [10]. It should be mentioned that the shear correction factor k in Eq. (5) was assumed to be unity, as C_{44} and C_{55} were directly predicted using micromechanics [3].

B. Top Facesheet Local Deflection

The top facesheet was directly exposed to a uniform pressure loading. The uniform pressure loading that acted on the thin facesheet resulted in local deflections that were not captured by the 2-D FSDT. The FSDT analysis resulted in midplane strains and curvatures at the center of the unit cell. The facesheet local deformation vector due to the pressure requires additional analysis. A 1-D beam problem was used to calculate the additional local deformation of the facesheet under uniform pressure load. Because of symmetry, only half of the top facesheet was analyzed (Fig. 4).

A matrix structural analysis method (FE) was used to determine the deflection of the top facesheet. Half of the top facesheet was modeled using two beam elements. Displacement and rotation boundary conditions were imposed on the two ends of the facesheet. A torsional spring element with a rotation boundary condition was used at the middle node to capture the resistance to rotation offered by the web connected to the facesheet. The elements are indicated by roman numerals in Fig. 4. Because of symmetry, θ_A and θ_c were zero. Because of the displacement constraint of the web and the facesheet, the deflection at junction B was set to zero, i.e., $v_B = 0$. The clamped boundary condition at node D resulted in θ_D being zero. The consistent, or work, equivalent loads on each element due to the uniform pressure loading were computed using the beam element shape functions [16] as shown below:

$$\begin{Bmatrix} F_i \\ C_i \\ F_j \\ C_j \end{Bmatrix} = -\int_0^L P_o \begin{Bmatrix} 1 - \frac{3\bar{y}_f^2}{L^2} + \frac{2\bar{y}_f^3}{L^3} \\ \bar{y}_f - \frac{2\bar{y}_f^2}{L} + \frac{\bar{y}_f^3}{L^2} \\ \frac{3\bar{y}_f^2}{L^2} - \frac{2\bar{y}_f^3}{L^3} \\ -\frac{\bar{y}_f^2}{L} + \frac{\bar{y}_f^3}{L^2} \end{Bmatrix} \mathrm{d}\bar{y}_f \tag{6}$$

In Eq. (6), i and j correspond to the left and right nodes of the beam and torsional elements, and L corresponds to the length of the beam element. The element stiffness matrix for the beam and torsional spring elements were assembled accordingly to obtain the global stiffness matrix and global force vector:

$$EI\begin{bmatrix} \frac{12}{L_1^3} & 0 & \frac{6}{L_1^2} \\ 0 & \frac{12}{L_2^3} & -\frac{6}{L_2^2} \\ \frac{6}{L_1^2} & -\frac{6}{L_2^2} & 4\left(\frac{1}{L_1}+\frac{1}{L_2}+\frac{1}{L_3}\right) \end{bmatrix} \begin{Bmatrix} v_A \\ v_C \\ \theta_B \end{Bmatrix} = \begin{Bmatrix} -\frac{P_o L_1}{2} \\ -\frac{P_o L_2}{2} \\ \frac{P_o L_1^2}{12} - \frac{P_o L_2^2}{12} \end{Bmatrix} \qquad [K]\{q\} = \{F\} \tag{7}$$

In Eq. (7), L_3 was the length of the web. Equation (7) was solved to obtain the nodal displacements, which were substituted back in the interpolation functions to obtain the transverse deflection of the facesheet:

$$v_I(\bar{y}_f) = \left(1 - \frac{3\bar{y}_f^2}{L^2} + \frac{2\bar{y}_f^3}{L^3}\right)v_A + \left(-\frac{\bar{y}_f^2}{L} + \frac{\bar{y}_f^3}{L^2}\right)\theta_B \tag{8}$$

$$v_{II}(\bar{y}_f) = \left(\bar{y} - \frac{2\bar{y}_f^2}{L} + \frac{\bar{y}_f^3}{L^2}\right)\theta_B + \left(\frac{3\bar{y}_f^2}{L^2} - \frac{2\bar{y}_f^3}{L^3}\right)v_C \tag{9}$$

The 1-D deflections from Eqs. (8) and (9) were superimposed with the plate deflection from Eq. (4a).

C. Stresses due to Pressure Loading

1. Stress Because of Midplane Strain and Curvature

The FSDT analysis of the equivalent plate yields midplane strains, curvatures, and transverse shear strains at given (x, y) of the equivalent plate. These deformations are called the macrodeformations [3], and they are the deformations in the equivalent orthotropic plate. To calculate the stresses in the ITPS, we apply the aforementioned macrodeformations to a unit cell situated at the same point. Then, using the transformation matrices defined by Martinez et al. [3], the (actual) deformations in the facesheets and the web were calculated. From the constitutive relations of the facesheet and web materials (layup in the cases of laminates), the stresses are calculated. A flowchart (Fig. 5) outlines the stress calculation procedure. In the flowchart, the x and y locations correspond to the ITPS 2-D equivalent plate, and $\bar{y}$ and $\bar{z}$ correspond the local location on either the face or web; Fig. 6a. If e in Fig. 5 was equal to 3 or 4 (left or right web), then the micro-mid-plane strains and curvatures were a

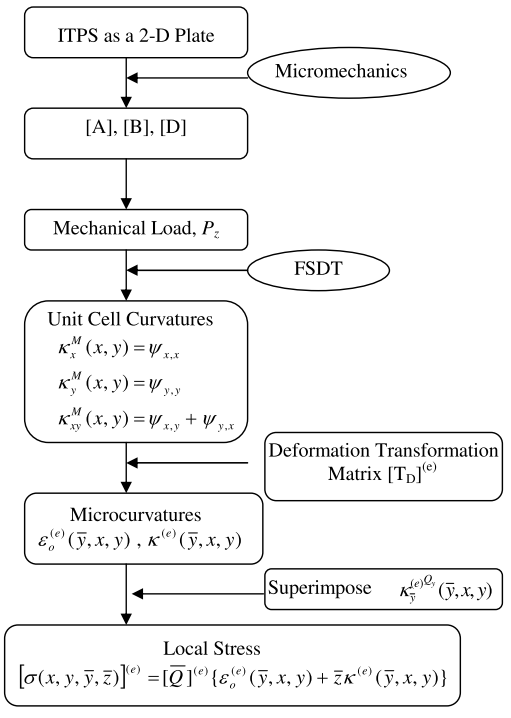

Fig. 5 Local stress flowchart for an ITPS as a 2-D plate with transverse shear force effects consideration.

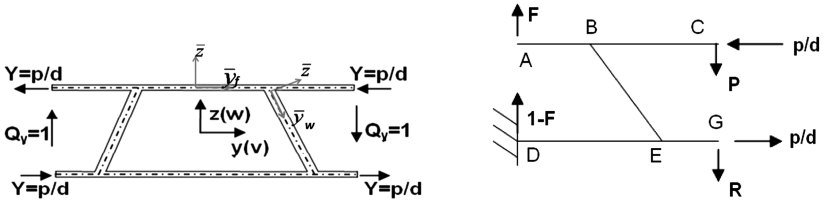

Fig. 6 Unit cells: a) ITPS unit cell under the action of transverse shear force, and b) half-ITPS unit cell.

function of $\bar{y}_w$, which would result in web stresses as a function of $\bar{y}_w$. There will be additional stresses in the top facesheet that result from the local effects of the pressure loading. These local stresses are determined from the local deflections derived in Eqs. (8) and (9) and added to that resulting from the equivalent plate analysis in Eq. (4). The stresses calculated from Eqs. (8) and (9) neglect a shear deformation term because the facesheets and webs are thin when considered by themselves and compared with the unit-cell dimensions.

2. Stress due to Transverse Shear Strains

In this section, we describe the procedures to calculate the stresses in the facesheets and web due to transverse shear force Q_y acting on the equivalent orthotropic plate. Figure 6 illustrates the ITPS half-unit cell under the action of various forces that resulted from a transverse shearing force Q_y. The unknown forces P, R, and F for unit Q_y were determined from Castigliano's second theorem [16]. Then, using the procedure described by Martinez et al. [15], the bending moments at a cross section of the facesheets or webs were determined (Appendix B). From the moment equations (Appendix B), the resulting curvature in either of the facesheets or webs was determined:

$$\kappa_{\bar{y}}^{(e)Q_y}(\bar{y}, x, y) = \left(\frac{-\bar{D}_{12}^{(e)}}{\bar{D}_{11}^{(e)}} + \bar{D}_{22}^{(e)}\right) M_{ij}(\bar{y}) Q_y(x, y) \qquad (10)$$

The flowchart shown in Fig. 5 takes into account the moments from Eq. (A1) and the transverse shear force from Eq. (A3) for local stress determination. The superscript e in Eq. (10) refers to a component assignment of the ITPS. An e of 1, 2, 3, and 4 refers to the top facesheet, bottom facesheet, left web, and right web. It should be mentioned that, in applying Castigliano's theorem, we accounted only for the strain energy due to bending in various segments of the cross sections. The energy due to in-plane forces and transverse shear force was assumed to be negligible compared with the bending energy since the thickness of the facesheet and webs are small when compared with its length.

3. Local Stress due to the Uniform Pressure Loading: One-Dimensional Analysis

The calculation of local stresses in the top facesheet due to pressure loading is a continuation of the analysis described above that determines the local transverse displacements [see Eqs. (8) and (9)]. The free body diagram of the top facesheet under the action of a uniform pressure loading is shown in Fig. 7.

In Fig. 8, the moments at points A and B were determined by multiplying the element stiffness matrix with the corresponding node displacement vector; see Appendix C.

The stresses at any local point of the top facesheet were determined by multiplying the moment vector with the inverse of the bending stiffness matrix and the lamina stiffness matrix of the facesheet as shown below. A superscript value of 1 refers to the top facesheet:

$$\begin{bmatrix} \sigma_{xx}(\bar{y}_f, \bar{z}_f) \\ \sigma_{yy}(\bar{y}_f, \bar{z}_f) \\ \tau_{yy}(\bar{y}_f, \bar{z}_f) \end{bmatrix}^{(1)} = \bar{z}_f \begin{bmatrix} \bar{Q}_{11}^{(1)} & \bar{Q}_{12}^{(1)} & \bar{Q}_{16}^{(1)} \\ \bar{Q}_{12}^{(1)} & \bar{Q}_{22}^{(1)} & \bar{Q}_{26}^{(1)} \\ \bar{Q}_{16}^{(1)} & \bar{Q}_{26}^{(1)} & \bar{Q}_{66}^{(1)} \end{bmatrix} \begin{bmatrix} D_{11}^{(1)} & D_{12}^{(1)} & D_{16}^{(1)} \\ D_{12}^{(1)} & D_{22}^{(1)} & D_{26}^{(1)} \\ D_{16}^{(1)} & D_{26}^{(1)} & D_{66}^{(1)} \end{bmatrix}^{-1} \begin{bmatrix} \frac{D_{12}^{(1)}}{D_{22}^{(1)}} M_{\bar{y}}^{ij} \\ M_{\bar{y}}^{ij} \\ 0 \end{bmatrix} \qquad (11)$$

D. Unsymmetric Integrated Thermal Protection System Panel Configuration

The methods described so far are for an ITPS with symmetric facesheet configurations with respect to the unit-cell y axis, i.e., $[B]$ matrix is zero. However, certain designs may call for different materials or thicknesses for the top and bottom facesheets that make it perform at its optimum for mechanical and thermal applications. Ceramic matrix composites and high-temperature metals are possible choices for the top facesheet due to their high service temperatures. Aluminum alloys and composite materials are of preference for the bottom facesheet due to their high specific heats and mass-efficient structural properties. An ITPS with different materials for the top and bottom facesheets results in a stiffness matrix with a nonzero coupling stiffness matrix, $[B] \neq 0$. This type of ITPS configuration will be referred to as an unsymmetric ITPS. The presence of the bending-extensional coupling stiffness matrix causes considerable difficulty in obtaining solutions to a plate problem using either the FSDT or CLPT method. As an alternative, the reduced stiffness matrix approach [14], wherein $[B]$ is assumed to be equal to zero and $[D]$ is modified, could be used. Then, the techniques described above for analysis of orthotropic plates can be directly used. The reduced stiffness matrix [Eq. (12)] was used in the plate solution of an orthotropic plate with a uniform pressure load. The use of the reduced stiffness matrix tends to reduce the effective stiffness

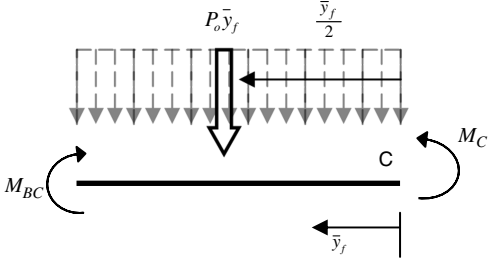

Fig. 7 Free body diagram of section BC (see Fig. 4) of the top facesheet.

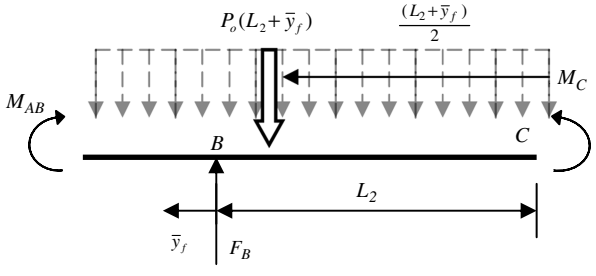

Fig. 8 Free body diagram of section AB (see Fig. 4) of the top facesheet.

of the plate, which results in increased bending deflections while buckling loads are decreased when compared with equivalent symmetric orthotropic plates. The corresponding error in the out-of-plane plate displacement and local stresses was investigated and compared with the FE results. The reduced bending stiffness matrix $[D^*]$ is given by [14]:

$$[D^*] = [D] - [B][A]^{-1}[B] \tag{12}$$

E. Thermal Stress Moment Resultants

The ITPS panel is exposed to extreme reentry temperatures that result in various temperature distributions through the ITPS thickness as a function of reentry time (transient heat transfer) [17]. The temperature distribution causes the ITPS to deform due to the resulting thermal force and moments that were determined by Martinez et. al [18]. An analytical solution was derived to predict the thermal deflection of the ITPS panel when subjected to a through-the-thickness temperature distribution. A 2-D plate analysis was needed to determine the response of the ITPS when it was subjected to thermal moments. Consider a rectangular plate simply supported along the nonloaded edges and bent by moments distributed along the edges $x = [0, a]$ (Fig. 9).

The distributed moment in Fig. 9 is equal to the previously calculated thermal moment from Martinez et al. [18]. Typical ranges of L/h for the ITPS will be from 10 to 20, which result in nonnegligible shear effects. An FSDT approach was implemented for the deflection solution of the ITPS plate. The boundary conditions for the thermal plate problem are as follows:

$$w = 0; \qquad \psi_x = 0 \qquad y = [0, b] \qquad w = 0; \qquad \psi_y = 0$$
$$x = [0, a] \qquad M_x^T = -D_{11}\psi_{x,x} \qquad x = [0, a] \tag{13}$$

The deflections and rotations are assumed such that they satisfy all displacement boundary conditions along the edges $y = 0$ and $y = b$:

$$w(x, y) = \sum_{n=1}^{N} A_n(x) \sin\frac{n\pi y}{b} \qquad \psi_x(x, y) = \sum_{n=1}^{N} B_n(x) \sin\frac{n\pi y}{b}$$
$$\psi_y(x, y) = \sum_{n=1}^{N} C_n(x) \cos\frac{n\pi y}{b} \tag{14}$$

The deflection and curvature solutions of the plate are taken in the form of a series where $A_n(x)$, $B_n(x)$, and $C_n(x)$ are all unknown functions of x only. It was assumed that the two unloaded edges are simply supported; hence, each term of the series satisfies the boundary conditions $w = 0$ and $\psi_x = 0$ on these two sides. It remains to determine $A_n(x)$, $B_n(x)$, and $C_n(x)$ in such a form to satisfy the boundary conditions on the sides $x = 0$ and $x = a$, and the equation of equilibrium [Eq. (A1)]. Taking the assumed deflection and rotations in the form of a series and substituting them into the equilibrium equations results in three ordinary differential equations [Eq. (D1)].

We assume solutions to be of the form of an exponential series function; see Eq. (D2). Substituting the assumed solution from Eq. (D2) in the differential equations [Eq. (D1)] yields a set of homogeneous linear equations for the unknown coefficients α, β, and γ as shown below:

$$\det\begin{bmatrix} -D_{11}\lambda^2 + D_{66}\eta^2 + A_{55} & (D_{12} + D_{66})\lambda\eta & A_{55}\lambda \\ (D_{12} + D_{66})\lambda\eta & D_{66}\lambda^2 - D_{22}\eta^2 - A_{44} & -A_{44}\eta \\ A_{55}\lambda & -A_{44}\eta & A_{55}\lambda^2 - A_{44}\eta^2 \end{bmatrix} \times \begin{Bmatrix} \beta \\ \gamma \\ \alpha \end{Bmatrix} = \begin{Bmatrix} 0 \\ 0 \\ 0 \end{Bmatrix} \tag{15}$$

The lambdas were solved by setting the determinant of the coefficient matrix to zero. The solution to Eq. (15) yielded six solutions $(\lambda, -\lambda_6)$. The six roots yielded six terms in Eq. (D2), which resulted in three equations with six unknowns per equation [Eqs. (D3–D5)]. Eighteen unknown constants resulted from the equations in Appendix D, which were not possible to solve with only six boundary conditions. However, a relation was made between all 18 constants (see Appendix D), which reduced the number of independent constants from 18 to 6. A unique solution to each unknown constant was now available because of the equal number of unknown constants and boundary conditions.

The moment distribution along the edges of the plate was represented by the Fourier sine series as

$$M_x = \sum_{n=1}^{N} M_n \sin\frac{n\pi x}{a} \tag{16}$$

For the case of a uniform distribution of the bending moments, the term M_n was represented as $M_n = 4M_x^T/n\pi$. A system of six linear equations was obtained by substituting Eq. (D2) into Eq. (14) and Eq. (14) into Eq. (13):

$$\begin{Bmatrix} \alpha_1 \\ \alpha_2 \\ \alpha_3 \\ \alpha_4 \\ \alpha_5 \\ \alpha_6 \end{Bmatrix} = \begin{bmatrix} 1 & 1 & 1 & 1 & 1 & 1 \\ e^{\lambda_1 b} & e^{\lambda_2 b} & e^{\lambda_3 b} & e^{\lambda_4 b} & e^{\lambda_5 b} & e^{\lambda_6 b} \\ \bar{C}_1 & \bar{C}_2 & \bar{C}_3 & \bar{C}_4 & \bar{C}_5 & \bar{C}_6 \\ \bar{C}_1 e^{\lambda_1 b} & \bar{C}_2 e^{\lambda_2 b} & \bar{C}_3 e^{\lambda_3 b} & \bar{C}_4 e^{\lambda_4 b} & \bar{C}_5 e^{\lambda_5 b} & \bar{C}_6 e^{\lambda_6 b} \\ -D_{22}\bar{D}_1\lambda_1 & -D_{22}\bar{D}_2\lambda_2 & -D_{22}\bar{D}_1\lambda_3 & -D_{22}\bar{D}_1\lambda_4 & -D_{22}\bar{D}_1\lambda_5 & -D_{22}\bar{D}_1\lambda_6 \\ -D_{22}\bar{D}_1\lambda_1 e^{\lambda_1 b} & -D_{22}\bar{D}_1\lambda_1 e^{\lambda_1 b} & -D_{22}\bar{D}_1\lambda_1 e^{\lambda_1 b} & -D_{22}\bar{D}_1\lambda_1 e^{\lambda_1 b} & -D_{22}\bar{D}_1\lambda_1 e^{\lambda_1 b} & -D_{22}\bar{D}_1\lambda_1 e^{\lambda_1 b} \end{bmatrix}^{-1} \begin{Bmatrix} 0 \\ 0 \\ 0 \\ 0 \\ \frac{4M_y^T}{m\pi} \\ \frac{4M_y^T}{m\pi} \end{Bmatrix} \tag{17}$$

By solving the set of six linear equations, the assumed deflection equations [Eq. (15)] were solved. Equations (D6) and (D7) were used to obtain the solutions to the plate rotation in the x and y directions. The same procedure was applicable for uniformly distributed

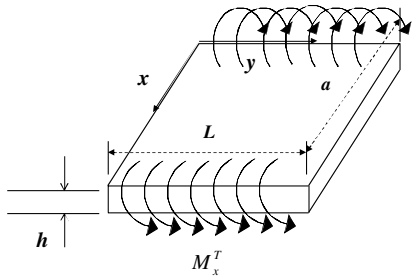

Fig. 9 ITPS orthotropic plate subjected to uniformly distributed thermal end moments.

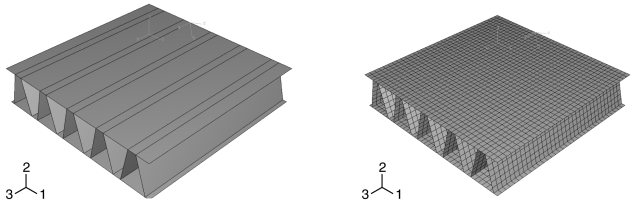

Fig. 10 FE a) model and b) mesh.

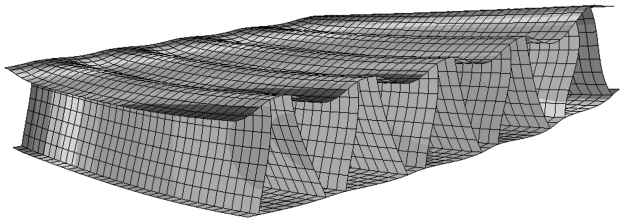

Fig. 12 ITPS out-of-plane deformation.

bending moments along the y axis. In the case of simultaneous action of couples along the entire boundary of the ITPS plate, the deflections and moments can be obtained by suitable superposition of the results obtained from the detailed discussion.

III. Results

A. Integrated Thermal Protection System Out-of-Plane Displacement: Pressure Load

For verification of the accuracy in prediction of the deflection and stress results of an ITPS sandwich panel under the action of a uniform pressure loading, an ITPS panel with the following dimensions was analyzed: $p = 50$ mm, $d = 100$ mm, $t_{\mathrm{TF}} = 1.5$ mm, $t_{\mathrm{BF}} = 1.5$ mm, $t_w = 1.5$ mm, $\theta = 75°$, $a = 1$ m, and $b = 1$ m. An Inconel 617 alloy was used as an example to verify the analytical models for determining local stresses in the ITPS sandwich panel ($E = 202$ GPa, $\nu = 0.287$). A 10-unit-cell ITPS sandwich panel was modeled for the analysis (Fig. 10a). Because of symmetry of the ITPS panel, only a quarter of the plate was modeled. A 3-D FE analysis was conducted on the ITPS plate using the commercial ABAQUS$^{\mathrm{TM}}$ version 6.4 FE program. Eight node shell elements were used to model the facesheets and webs of the unit cell. The shell elements have the capability to include multiple layers of different material properties and thicknesses that are needed to model a laminate. Three integration points were used through the thickness of the shell elements. The FEM model consisted of 15,048 nodes and 5100 elements (Fig. 10b). The ITPS panel was subjected to a uniform pressure loading of 68,947 Pa (10 psi), and symmetric boundary conditions were imposed at the edges of the ITPS plate. The bottom facesheet had an out-of-plane displacement constraint $w(0, y) = w(x, 0) = 0$, while the top facesheet only had a rotation constraint in all three directions along $x = 0$ and $y = 0$ (Fig. 11). The FE model was constrained with the appropriate boundary conditions from Eq. (2) and appropriate symmetric boundary conditions. The y-symmetric boundary conditions are

$$v(x, b/2) = R_x(x, b/2) = R_z(x, b/2) = 0$$

and the x-symmetric boundary conditions are

$$u(a/2, 0) = R_x(a/2, 0) = R_z(a/2, 0) = 0$$

The FEM out-of-plane displacements of the ITPS panel at $x = a/2$ were extracted and compared with the results obtained from Eqs. (4a), (8), and (9). The homogenized ITPS 2-D plate can potentially have an unlimited number of fictitious unit cells depending on what x and y points are chosen. Since the FEM ITPS model contained 10 unit cells, for comparison, the homogenized ITPS 2-D plate was divided into a 10×10 grid. The accuracy was verified through FE results and a convergence study. Each intersection of the grid lines corresponded to an analytical ITPS unit cell that corresponded to the center location of the FEM unit cell. The curvatures in the x and y directions at each analytical grid intersection were assumed to be constant for the entire unit cell; however, the curvatures in the x and y directions from the 3-D FEM results were not constant within each unit cell. The curvatures varied through each unit cell. This stress gradient effect could not be captured by the analytical homogenized plate model. The FEM out-of-plane displacement contour of the ITPS is illustrated in Fig. 12. The FEM out-of-plane displacement results at $x = a/2$ were compared with

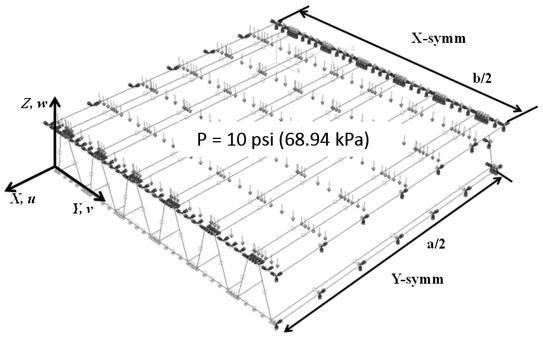

Fig. 11 FE boundary conditions for the ITPS plate.

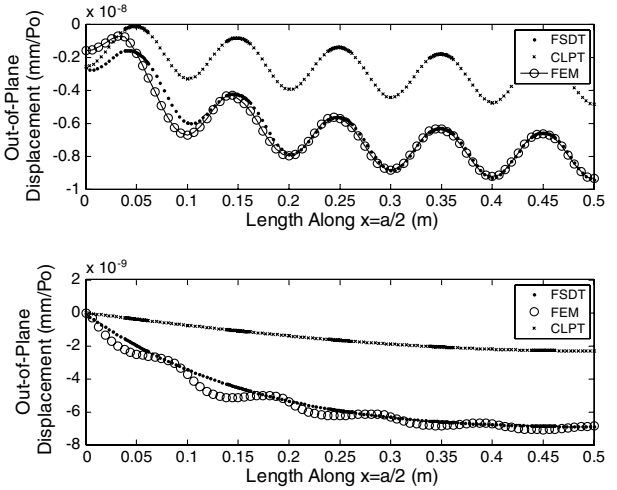

Fig. 13 Out-of-plane displacement comparison between FEM and analytical solution of the top and bottom facesheets.

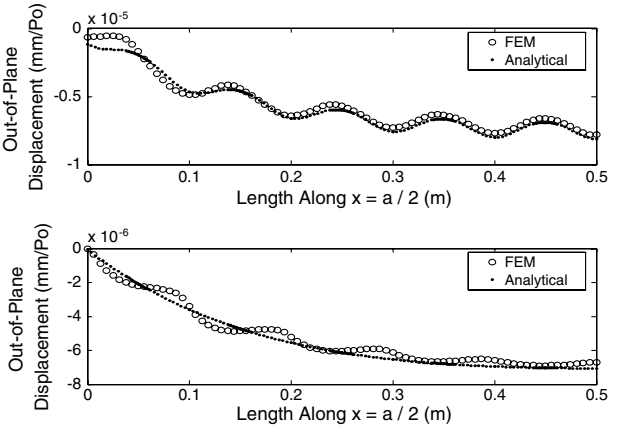

Fig. 14 Out-of-plane displacement comparison between FEM and analytical solution of the top and bottom facesheets for an unsymmetric ITPS.

Table 1 Thermal moments of Inconel 617 under the 450 s reentry temperature distribution

Stiffness	M_x, Nm/m	M_y, Nm/m
Analytical	1.20E + 05	8.84E + 04
FE	1.12E + 05	9.07E + 04
% diff.	7.1	2.5

the analytical results (Fig. 13). As seen in Fig. 13, the analytical out-of-plane displacement results are within a 1–2% difference from the FEM results. There was greater percentage difference near the boundary of the ITPS because the boundary conditions created localized effects that were not captured by the FSDT method and the 1-D beam analysis. At the center of the ITPS plate, the structure acted more like the homogenized 2-D plate because it was farther away from the boundary. The superposition of the displacement results obtained from the FSDT method and the 1-D beam analysis resulted in a less than 5% difference and an accurate representation of the top facesheet deflection response when subjected to a uniform pressure load. The bottom facesheet FE displacement results agreed well with the displacement results obtained from the FSDT method. The bottom facesheet deflection acted more like a 2-D plate because of the absence of local effects from the uniform pressure loading.

To verify the applicability of present methods to unsymmetric ITPS, an ITPS with a different bottom facesheet was considered. The bottom facesheet was assumed to be of an aluminum alloy ($E=$ 72.519 GPa, $\nu_{12} = 0.30$). An ITPS panel with the same dimensions as mentioned above was modeled and analyzed for investigation of the error in using the reduced stiffness matrix in the FSDT method for an unsymmetric ITPS panel. The FEM local stresses were extracted at $x = a/2$ and compared with the analytical stresses that resulted from the FSDT method by use of the reduced stiffness matrix. From Fig. 14, it can be noted that the plate displacement results were not affected by using the reduced stiffness matrix in the FSDT plate analysis. The largest difference between the FEM and analytical results was less than 5%.

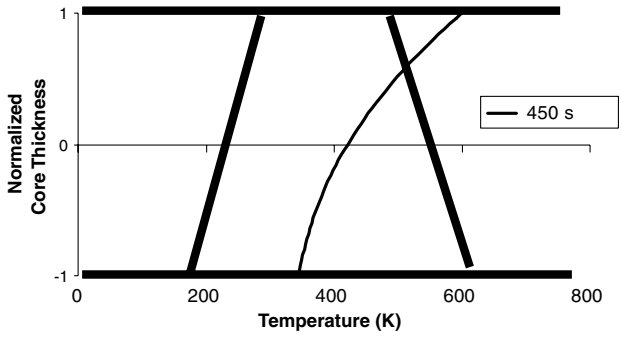

Fig. 15 ITPS temperature distribution at 450 s reentry time.

Table 2 Boundary conditions of the ITPS panel

	Top face rotation	Top face displacement	Bottom face rotation	Bottom face displacement
Boundary condition 1	X		X	X
Boundary condition 2	X			X
Boundary condition 3			X	X

B. Integrated Thermal Protection System Out-of-Plane Displacement: Temperature Distribution

From the results obtained by Martinez [19] on the analysis of a plate under the action of thermal edge moments, confidence was gained with the analytical procedure for a plate solution of an orthotropic thick plate under the action of uniformly distributed edge moments. The next step was to apply that approach to analytically predict the out-of-plane displacement of an ITPS under the action of thermal moments from an applied temperature distribution. The temperature distribution that was considered for the analysis was at the 450 s reentry time of a space-shuttle-type vehicle, as described in [19] (Fig. 15). The ITPS was composed of Inconel 617, and the resulting thermal moments for Inconel 617 are calculated and compared with the FE verification procedure discussed by Martinez [19]. The greatest percentage difference between the analytical and FEM comparison was less than 7% for M_x^T. The thermal moment results (Table 1) were used to determine the analytical out-of-plane displacement of the ITPS panel. Table 1 consists of two moments. The aforementioned thermal plate analysis with edge moments on the x and y axes can be used through suitable superposition (see Fig. 16).

The same ITPS panel that was modeled for the pressure load example was used for the temperature distribution example, except for this case, the thickness of the faces and webs was increased from 1.5 mm (0.059 in.) to 2.0 mm (0.07874 in.). The number of nodes and elements remained the same, as well as the boundary conditions. The 450 s temperature distribution was included in the FEM input file, and the out-of-plane displacement of the ITPS was extracted at $x = a/2$ after analysis. There was no need to do any local out-of-plane displacement problem for this case because the temperatures of the top and bottom facesheets were considered to be constant because of the thin faces when compared with the ITPS thickness. Therefore, the faces were only under the action of a thermal expansion.

The out-of-plane displacement FEM result of the ITPS panel under the action of the fourth-order temperature distribution is shown in Fig. 16 along with the CLPT [19] and FSDT analytical results. The FSDT method for predicting out-of-plane displacement for an ITPS under the action of uniformly distributed edge moments does not predict accurate results for this particular ITPS panel. The FSDT method overpredicts the actual FE displacement by 50%, and the CLPT [20] method underpredicts the actual FE displacement by

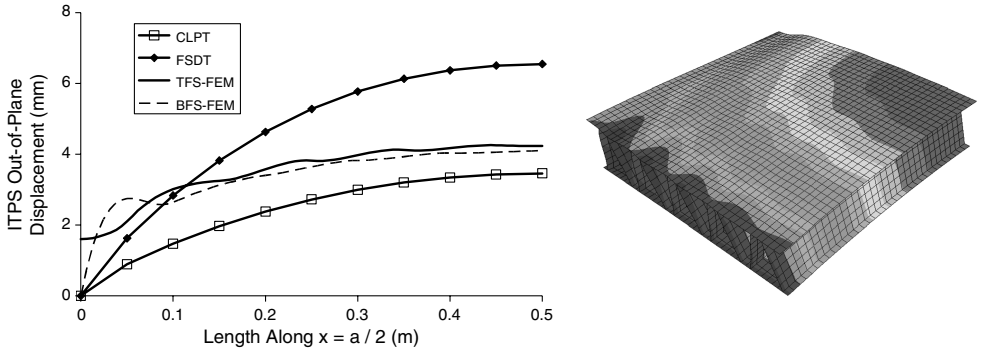

a) b)

Fig. 16 ITPS a) out-of-plane thermal displacement and b) thermal displacement contour (TFS denotes top facesheet; BFS denotes bottom facesheet).

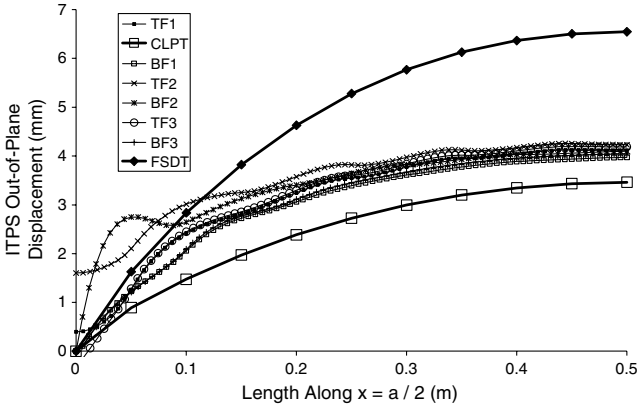

Fig. 17 ITPS out-of-plane displacement due to a fourth-order temperature distribution for various edge boundary conditions.

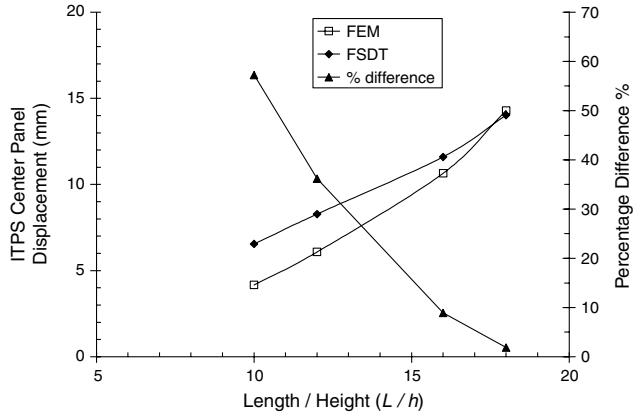

Fig. 18 ITPS center panel displacement for various L/h values.

20%. The edge boundary conditions of the top and bottom facesheets of the FEM model were modified in hopes of obtaining a good comparison between the FEM and analytical results. The set of boundary conditions are listed in Table 2. An "X" represents a constrained condition.

The ITPS out-of-plane displacement results for all different boundary conditions are shown in Fig. 17 and compared with the CLPT and FSDT results. As seen from Fig. 17, the boundary condition does not affect the center plate out-of-plane displacement. The different boundary conditions had an effect on the out-of-plane displacements that were near the edge boundary. The different boundary conditions cause different boundary effects that affect the ITPS out-of-plane displacement that cannot be captured by the FSDT or CLPT methods. The change in boundary condition did not lead to a better comparison between the FEM and analytical results.

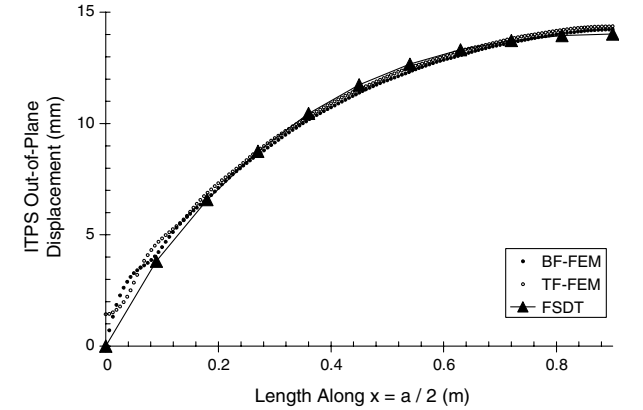

Fig. 19 ITPS out-of-plane displacement due to a temperature distribution for an ITPS with $L/h = 18$.

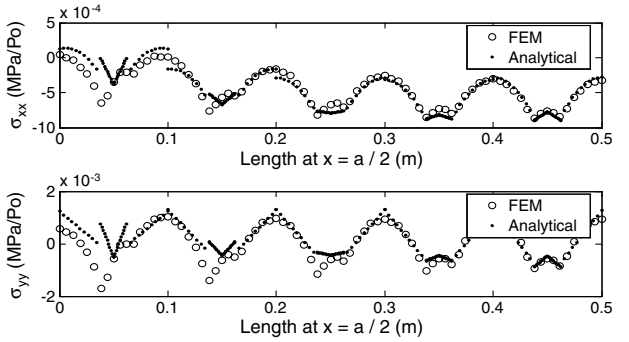

Fig. 20 Top facesheet stress in the x and y directions of the ITPS panel.

The thermal moments that resulted from the fourth-order temperature distribution caused the ITPS panel to bend due to thermal stresses. Since the ITPS plate had a low L/h value, the thermal moments acted on a short edge length of the ITPS, which introduced other local boundary effects into the results. These local ITPS plate effects that resulted from the thermal moments were not fully captured by the FSDT and CLPT methods when the plate had a low L/h ratio. The L/h ratio of the ITPS was increased to investigate what L/h ratio of an ITPS will result in a less than a 5% prediction error of the FEM and analytical out-of-plane thermal displacement results. The L/h ratio in the FEM model was increased by adding more unit cells to the ITPS plate while keeping the ITPS thickness constant. For ITPS plates with large L/h ratios, the thermal moments now acted on a long edge length, and all the local ITPS boundary effects were minimized. The ITPS panel was able to bend as a plate, and the bending behavior was captured by the FSDT that was outlined above. The resulting maximum out-of-plane displacement was extracted from the FEM output after analysis and compared with the maximum analytical plate displacement for various L/h ratios. The percentage error decreased from 50% for low L/h ratios to 2% for high L/h ratios (Fig. 18). The analytical and FEM results were in good agreement for that particular L/h ratio, which resulted in a less than 5% prediction error of the ITPS out-of-plane displacement from a fourth-order temperature distribution (see Fig. 19). The FEM and analytical stress results were plotted at $x = a/2$ for an ITPS panel with an $L/h = 18$ (Figs. 20 and 21).

C. Integrated Thermal Protection System Local Stress

The FEM local stresses in the x and y directions were extracted from the FEM output after analysis at $x = a/2$. The analytical top facesheet stresses were computed by superimposing the stresses results from Fig. 5 and Eq. (17). The bottom facesheet and web stresses were computed from Fig. 5. All stress results were computed at $\bar{z}_{f \text{ or } w} = -t/2$, which was the bottom surface of each component. Similar to the out-of-plane displacement results, the percentage difference between the FEM and analytical results was greater at the boundary of the ITPS; see Figs. 20–22. The percentage difference near the boundary of the ITPS was 9%. The percentage difference

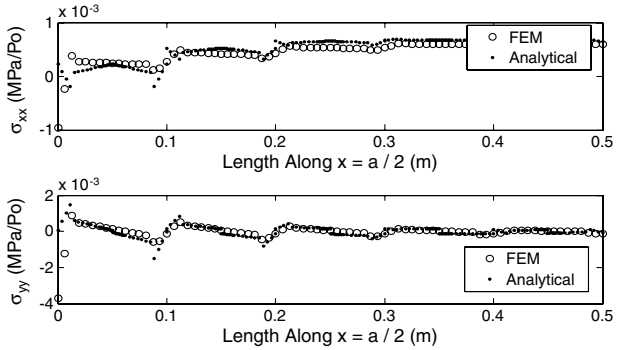

Fig. 21 Bottom facesheet stress in the x and y directions of the ITPS panel.

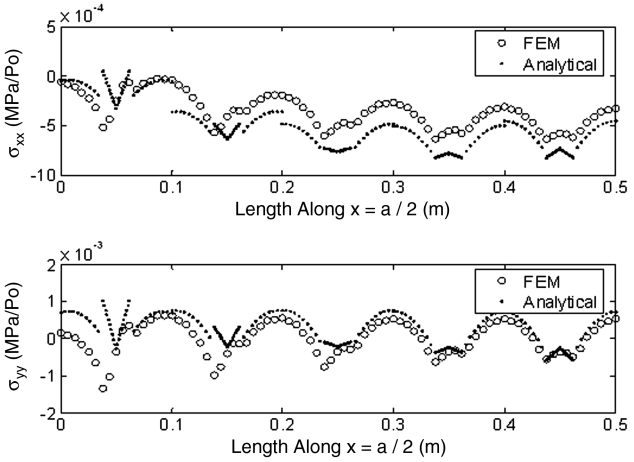

Fig. 22 Top facesheet stress in the *x* and *y* directions of an unsymmetric ITPS panel.

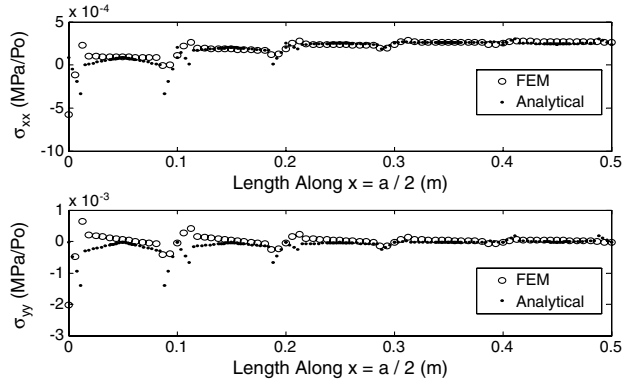

Fig. 23 Bottom facesheet stress in the *x* and *y* directions of an unsymmetric ITPS panel.

was less than 2% for stress results near the center of the ITPS plate. The percentage difference for the web stress in the x direction was less than 1% when compared with the FEM results. The percentage difference for the web stresses in the y direction was less than 3% at the center of the plate and greater than 5% near the boundary of the ITPS panel. The analytical local stress of the right web in the $\bar{y}_w$ direction was different than the FEM results because, near the boundary of the ITPS, there was a large change in curvature due to the local boundary effect that was not captured by the analytical model. The curvature was changing through the length of the unit cell while, in the analytical model, the curvature was kept constant. The local stress prediction gets better when the local stresses are compared at the center of the plate. There are less boundary effects, and the curvature can be assumed constant for a unit cell.

For investigation of the penalty of using the reduced stiffness matrix in the FSDT method for an unsymmetric ITPS panel, an unsymmetric panel with the same dimensions as mentioned above was modeled and analyzed. The difference in this new model was that the top facesheet and webs were composed of Inconel 617, and the bottom facesheet was composed of an aluminum alloy ($E=$ 72.519 GPa, $\nu_{12} = 0.3$). The FEM local stresses were extracted at $x = a/2$ and compared with the analytical stresses that resulted from the FSDT method by use of the reduced stiffness matrix. The comparison between the FE results and the stress results obtained from the FSDT method are illustrated in Figs. 22 and 23. The results indicated that there was a 20% difference between the analytical and FE results in the top facesheet when using the reduced stiffness matrix. The use of the reduced stiffness matrix in the FSDT method did not have any effect on the bottom facesheet and web stresses when compared with the FEM results. The difference was much more noticeable in the top facesheet because of the local effects that resulted from the uniform pressure load.

IV. Conclusions

A 2-D plate solution for determining out-of-plane displacement of an orthotropic thick plate was established and verified with FEM for a uniform pressure load and uniform thermal edge moments. Additional local facesheet deformations and stress were superimposed with the 2-D plate results to capture the local effects of the distributed pressure load on the facesheets. Kirchhoff hypotheses and Euler–Bernoulli plate equations were used for the local displacement and stress analysis of the facesheets and webs. The symmetric and unsymmetric plates resulted in a less than 5% prediction error in the plate's out-of-plane displacements when compared with the FEM. The plate solution provided less than 5% prediction error results for ITPS panels with L/h ratios greater than 18. An ITPS panel with a low L/h introduced local boundary effects that contributed to the panel's out-of-plane displacement. A 1-D beam analysis was done on the top facesheet to account for the local bending of the top facesheet due to its thin thickness. The local boundary effects that introduced local displacements and stresses were not fully captured with either the FSDT method or the CLPT method.

Appendix A: Plate Equilibrium Equations and Constitutive Relations

The plate equilibrium equations are

$$\frac{\partial M_x}{\partial x} + \frac{\partial M_{xy}}{\partial y} - Q_x = 0 \qquad \frac{\partial M_{xy}}{\partial x} + \frac{\partial M_y}{\partial y} - Q_y = 0$$
$$\frac{\partial Q_x}{\partial x} + \frac{\partial Q_y}{\partial y} + P_z = 0 \tag{A1}$$

The plate constitutive relations are

$$\begin{Bmatrix} M_x \\ M_y \\ M_{xy} \end{Bmatrix} = \begin{bmatrix} D_{11} & D_{12} & 0 \\ D_{12} & D_{22} & 0 \\ 0 & 0 & D_{66} \end{bmatrix} \begin{Bmatrix} \psi_{x,x} \\ \psi_{y,y} \\ \psi_{x,y} + \psi_{y,x} \end{Bmatrix} \tag{A2}$$

$$\begin{Bmatrix} Q_y \\ Q_x \end{Bmatrix} = k \begin{bmatrix} C_{44} & 0 \\ 0 & C_{55} \end{bmatrix} \begin{Bmatrix} \psi_y + w_{,y} \\ \psi_x + w_{,x} \end{Bmatrix} \tag{A3}$$

Appendix B: Moments in the Half-Unit Cell

In this Appendix, we provide the expressions for bending moments in various parts of the unit cell due to unit transverse force [see Eq. (10)]. The detailed derivations can be found in [20]:

$$M_{AB}(\bar{y}) = F\bar{y} \qquad 0 \le \bar{y} \le f \tag{B1}$$

$$M_{BC}(\bar{y}) = P\bar{y} \qquad 0 \le \bar{y} \le p - f \tag{B2}$$

$$M_{DE}(\bar{y}) = (1 - F)\bar{y} - (P + R)p - Jd \qquad 0 \le \bar{y} \le p - f \tag{B3}$$

$$M_{EG}(\bar{y}) = R\bar{y} \qquad 0 \le \bar{y} \le f \tag{B4}$$

$$M_{BE}(\bar{y}) = F(f + \bar{y}\cos\theta) + P(p - f - \bar{y}\cos\theta) - H\bar{y}\sin\theta$$
$$0 \le \bar{y} \le s \tag{B5}$$

Appendix C: Local Bending Stress in Facesheets due to a Uniform Pressure Loading

The moments in the equations shown below are the result of the uniform pressure loading acting on the top facesheet. The moments were obtained from a 1-D FE analysis. The moments were multiplied

with the bending stiffness matrix of the facesheet to obtain facesheet stress:

$$M_C = \frac{EI}{L_2^3}(2L_2^2\theta_B - 6L_2 v_B) \tag{C1}$$

$$M_A = \frac{EI}{L_1^3}(6L_1 v_A + 2L_1^2\theta_B) \tag{C2}$$

The bending moment distribution in the top facesheet consists of two equations:

$$M_{\bar{y}}^{BC}(\bar{y}) = M_C - P_o\frac{\bar{y}^2}{2} \qquad 0 \le \bar{y} \le p - f \tag{C3}$$

$$M_{\bar{y}}^{AB}(\bar{y}) = F_B\bar{y} + M_C - P_o\frac{(L_2+\bar{y})^2}{2} \qquad 0 \le \bar{y} \le f \tag{C4}$$

Appendix D: Edge Moments

In this section, the assumed solutions to the plate deflection with edge moments are provided. A relationship is also made to reduce the number of unknown constants from 18 to 6.

Ordinary differential equations to a 2-D plate with edge moments:

$$D_{11}B_n''(x) - (D_{66}\eta^2 + C_{55})B_n(x) - (D_{12}+D_{66})\eta C_n'(x) - C_{55}A_n'(x) = 0 \tag{D1a}$$

$$D_{66}C_n''(x) - (D_{22}\eta^2 + C_{44})C_n(x) - (D_{12}+D_{66})\eta B_n'(x) - C_{44}\eta A_n(x) = 0 \tag{D1b}$$

$$C_{55}A_n''(x) - C_{44}\eta^2 A_n(x) + C_{55}B_n'(x) - C_{44}\eta C_n(x) = 0 \tag{D1c}$$

$$A_n(x) = \sum_{i=1}^{N}\alpha_i e^{\lambda_i x} \tag{D2a}$$

$$B_n(x) = \sum_{i=1}^{N}\beta_i e^{\lambda_i x} \tag{D2b}$$

$$C_n(x) = \sum_{i=1}^{N}\gamma_i e^{\lambda_i x} \tag{D2c}$$

$$A_n(x) = \alpha_1 e^{\lambda_1 x} + \alpha_2 e^{\lambda_2 x} + \alpha_3 e^{\lambda_3 x} + \alpha_4 e^{\lambda_4 x} + \alpha_5 e^{\lambda_5 x} + \alpha_6 e^{\lambda_6 x} \tag{D3}$$

$$B_n(x) = \beta_1 e^{\lambda_1 x} + \beta_2 e^{\lambda_2 x} + \beta_3 e^{\lambda_3 x} + \beta_4 e^{\lambda_4 x} + \beta_5 e^{\lambda_5 x} + \beta_6 e^{\lambda_6 x} \tag{D4}$$

$$C_n(x) = \gamma_1 e^{\lambda_1 x} + \gamma_2 e^{\lambda_2 x} + \gamma_3 e^{\lambda_3 x} + \gamma_4 e^{\lambda_4 x} + \gamma_5 e^{\lambda_5 x} + \gamma_6 e^{\lambda_6 x} \tag{D5}$$

$$\beta_i = \alpha_i\left(\frac{k_{12}^i k_{23}^i - k_{22}^i k_{13}^i}{k_{22}^i k_{11}^i - k_{12}^i k_{21}^i}\right) = \bar{C}_i\alpha_i \tag{D6}$$

$$\gamma_i = \alpha_i\left(\frac{k_{13}^i k_{21}^i - k_{23}^i k_{11}^i}{k_{22}^i k_{11}^i - k_{12}^i k_{21}^i}\right) = \bar{D}_i\alpha_i \tag{D7}$$

$$k_{11}^i = -D_{11}\lambda_i^2 + D_{66}\eta^2 + C_{55} \tag{D8}$$

$$k_{22}^i = D_{66}\lambda_i^2 - D_{22}\eta^2 - C_{44} \tag{D9}$$

$$k_{21}^i = k_{12}^i = (D_{12}+D_{66})\lambda_i\eta \tag{D10}$$

$$k_{23}^i = -C_{44}\eta \tag{D11}$$

$$k_{13}^i = C_{55}\lambda_i \tag{D12}$$

Acknowledgments

This research is sponsored by a NASA grant under the Constellation University Institutes Project. The program manager is Claudia Mayer at NASA John H. Glenn Research Center at Lewis Field.

References

[1] Zhu, H., "Design of Metallic Foams as Insulation in Thermal Protection Systems," Ph.D. Dissertation, Univ. of Florida, Gainesville, FL, 2004.

[2] Blosser, M. L., "Advanced Metallic Thermal Protection Systems for Reusable Launch Vehicles," Ph.D. Dissertation, Univ. of Virginia, Charlottesville, VA, 2000.

[3] Martinez, O., Sankar, B. V., Haftka, R., Blosser, M., and Bapanapalli, S. K., "Micromechanical Analysis of a Composite Corrugated-Core Sandwich Panel for Integral Thermal Protection Systems," *AIAA Journal*, Vol. 45, No. 9, 2007, pp. 2323–2336. doi:10.2514/1.26779

[4] Martinez, O., Sharma, A., Sankar, B. V., Haftka, R., and Blosser, M. L., "Thermal Response Analysis of an Integrated Thermal Protection System for Future Space Vehicles," *AIAA Journal*, Vol. 48, No. 1, 2010, pp. 119–128. doi:10.2514/1.40678

[5] Fung, T. C., Tan, K. H., and Lok, T. S., "Analysis of C-Core Sandwich Plate Decking," *Proceedings of the 3rd International Offshore and Polar Engineering Conference*, Mountain View, CA, Vol. 4, 1993, pp. 244–249.

[6] Fung, T. C., Tan, K. H., and Lok, T. S., "Elastic Constants for Z-Core Sandwich Panels," *Journal of Structural Engineering*, Vol. 120, No. 10, 1994, pp. 3046–3065. doi:10.1061/(ASCE)0733-9445(1994)120:10(3046)

[7] Libove, C., and Hubka, R. E., "Elastic Constants for Corrugated Core Sandwich Plates," NACA TN-2289, 1951.

[8] Lok, T. S., Cheng, Q., and Heng, L., "Equivalent Stiffness Parameters of Truss-Core Sandwich Panel," *Proceedings of the Ninth International Offshore and Polar Engineering Conference*, Vol. 4, International Soc. of Offshore and Polar Engineers, Brest, France, 1999, pp. 292–298.

[9] Valdevit, L., Hutchinson, J. W., and Evans, A. G., "Structurally Optimized Sandwich Panels with Prismatic Cores," *International Journal of Solids and Structures*, Vol. 41, May 2004, pp. 5105–5124. doi:10.1016/j.ijsolstr.2004.04.027

[10] Lok, T. S., and Cheng, Q., "Elastic Stiffness Properties and Behavior of Truss-Core Sandwich Panel," *Journal of Structural Engineering*, Vol. 126, No. 5, May 2000, pp. 552–559. doi:10.1061/(ASCE)0733-9445(2000)126:5(552)

[11] Fung, T. C., Tan, K. H., and Lok, T. S., "Shear Stiffness DQy for C-Core Sandwich Panels," *Journal of Structural Engineering*, Vol. 122, No. 8, 1996, pp. 958–966. doi:10.1061/(ASCE)0733-9445(1996)122:8(958)

[12] Libove, C., and Batdorf, S. B., "A General Small Deflection Theory for Flat Sandwich Plates," NACA TN-1526, 1948.

[13] Whitney, M., *Structural Analysis of Laminated Anisotropic Plates*, Technomic, Lancaster, PA, 1987, Chaps. 7–9.

[14] Reddy, J. N., *Mechanics of Laminated Composite Plates Theory and Analysis*, CRC Press, Boca Raton, 1997, Chaps. 5–6.

[15] Martinez, O., Bapanapalli, S., Sankar, B. V., Haftka, R., and Blosser, M., "Micromechanical Analysis of a Composite Truss Core Sandwich Panel for Integral Thermal Protection Systems," 47th AIAA/ASME/ASCE/AHS/ASC Structures, Structural Dynamics, and Materials Conference, Newport, RI, AIAA Paper 2006-1876, May 2006.

[16] Sankar, B. V., and Kim, N. H., *Introduction to Finite Element Analysis and Design*, Wiley, NY, 2009, Chaps. 3–4.

[17] Bapanapalli, S. K., Martinez, O., Sankar, B. V., Haftka, R. T., and Blosser, M. L., "Analysis and Design of Corrugated-Core Sandwich Panels for Thermal Protection Systems of Space Vehicles," 47th AIAA/ASME/ASCE/AHS/ASC Structures, Structural Dynamics, and Materials Conference, Newport, RI, AIAA Paper 2006-1942, May 2006.

[18] Martinez, O., Sankar, B. V., and Haftka, R. T., "Thermal Response Analysis of an Integral Thermal Protection System for Future Space Vehicles," *ASME International Mechanical Engineering Congress and Exposition*, Chicago, IL, American Soc. of Mechanical Engineers Paper 2006-14522, Fairfield, NJ, Nov. 2006.

[19] Martinez, O., "Micromechanical Analysis and Design of an Integrated Thermal Protection System for Future Space Vehicles," Ph.D. Dissertation, Univ. of Florida, Gainesville, FL, 2007.

[20] Timoshenko, S., and Woinowsky-Kreiger, S., *Theory of Plates and Shells, Timoshenko*, McGraw–Hill, New York, 1959, pp. 180–185.

R. Ohayon
Associate Editor